Large-eddy simulations of droplet impingement on iced airfoils

By F. Zabaleta, S. T. Bose AND P. Moin

This study investigates droplet impingement using high-fidelity numerical simulations. We employ wall-modeled large-eddy simulations coupled with a Lagrangian particle model for droplet trajectories. The model is first validated against experimental data for a NACA 64A008 swept tail, demonstrating excellent agreement in collection efficiency distributions, particularly for large-droplet conditions. We then apply the validated model to a laser-scanned rime ice geometry on a NACA 23012 airfoil to investigate the impact of surface roughness on droplet impingement patterns. Our results reveal that while spanwise-averaged collection efficiency remains largely unaffected by surface roughness, significant local variations occur. These variations are strongly dependent on droplet size, with larger droplets showing more pronounced effects. Droplet collection efficiency is concentrated on upstream-facing surfaces of roughness elements, creating sheltered zones behind them, where collection efficiency significantly decreases. This preferential deposition leads to a self-reinforcing mechanism of roughness growth, providing insights into the formation of characteristic rime ice structures. Our findings highlight the importance of considering small-scale surface perturbations in accurately predicting the development of roughness features during ice accretion, contributing to a more comprehensive understanding of the ice growth process.

1. Introduction

The impingement of supercooled liquid droplets on aircraft surfaces is the initial step in the formation of in-flight ice, a phenomenon that poses a significant and well-documented threat to aviation safety. Ice accretion alters the aerodynamic profile of wings and control surfaces, leading to performance degradation through increased drag, reduced lift, and a higher stall speed (Gent *et al.* 2000). The historical impact of this hazard in the United States is substantial; a review of the years 1982–2000 linked in-flight icing to 583 accidents and more than 800 fatalities (Petty & Floyd 2004), and it continues to be a factor in modern aviation incidents (National Transportation Safety Board 2023). Depending on the ambient conditions, ice can form with two distinct morphologies: rime and glaze ice. Rime ice occurs when droplets freeze completely upon impact, a process typically associated with low ambient temperatures, low liquid water content (LWC), and small droplet sizes. Because the droplets solidify immediately, the resulting ice shape is determined predominantly by the droplet impingement distribution. Therefore, an accurate prediction of the impingement distribution is essential for correctly modeling the growth of rime ice. In contrast, glaze ice forms when only a fraction of a droplet's mass freezes upon contact, while the remainder forms a liquid film on the surface. This liquid water can then run back along the airfoil, freezing at a different location or being shed entirely, often leading to the formation of complex structures such as horns. Consequently, rather than depending solely on the initial impingement distribution, the growth of glaze ice is strongly governed by the underlying heat transfer processes (Zabaleta *et al.* 2025a).

The prediction of aircraft icing relies on a numerical framework that leverages the large separation of timescales between the slow ice growth process and the much faster aerodynamic and droplet dynamics. Representing the ice growth as a series of quasi-steady steps allows a multistep/shot process to be employed. First, the aerodynamic flow field around the geometry is computed (often using Reynolds-averaged Navier–Stokes closures). The resulting velocity field is then used to solve a droplet transport model, which yields the local collection efficiency, quantifying the rate of particle impingement on the surface. This collection efficiency then serves as an input to a thermodynamic model, where mass and energy conservation equations are solved over the airfoil/ice surface (Messinger 1953; Myers 2001) to determine the local ice growth rate. For a multishot simulation, this rate is used to evolve the surface geometry, and the entire sequence is repeated for each subsequent time step/shot.

Droplet dynamics are described through either an Eulerian–Lagrangian approach (Shad *et al.* 2025) or an Eulerian–Eulerian approach (Bellosta *et al.* 2023). The Lagrangian method tracks the trajectory of individual particles or parcels, facilitating the straightforward incorporation of particle–wall interaction effects, such as splashing. However, the Eulerian–Lagrangian framework often requires tracking of a large number of particles, making it computationally expensive for three-dimensional geometries and complex flow fields. Alternatively, the Eulerian–Eulerian description models the dispersed phase as a continuous medium, offering continuity of the solution and often achieving lower computational costs for large three-dimensional configurations, albeit with difficulties in accurately accounting for secondary splashing droplets and shadow regions (Guardone *et al.* 2025).

While this quasi-steady, multishot framework can effectively predict the mean profile of rime ice accretions, as demonstrated in the 1st AIAA Ice Prediction Workshop (IPW 1) (Laurendeau *et al.* 2022), a significant shortcoming is their failure to predict the small-scale surface roughness characteristic of real ice. This idealization to a smooth surface represents a significant limitation, as roughness is responsible for an increase in skin friction, heat transfer, and early transition to turbulence. To bridge this gap, empirical models are used to account for the effects of roughness, typically by approximating the nonhomogeneous surface with an equivalent sand grain roughness, k_s. This parameter is derived from empirical models, which can be based on either experimental correlations (Ignatowicz *et al.* 2023) or simplified bead dynamics modeling that represents the freezing of individual droplets (Ozcer *et al.* 2011).

The aerodynamic significance of these small-scale features has been the subject of recent investigation. Bellosta *et al.* (2024) demonstrated that the aerodynamic degradation associated with rime ice shapes is caused primarily by roughness. Specifically, when they analyzed a progressively smoothed version of a laser-scanned rime ice shape, they found that removing the smallest roughness scales significantly altered the aerodynamic behavior, with performance metrics approaching those of a clean airfoil. Furthermore, the underlying flow physics diverge significantly between smooth and rough shapes. Bornhoft *et al.* (2025) noted that simulations on smooth ice shapes can introduce flow features like laminar separation, which are absent on real, rough surfaces where the boundary layer immediately transitions to turbulence. This divergence in physics, coupled with the aerodynamic sensitivity to small-scale features, highlights the challenge of predicting performance penalties from smooth, numerically predicted shapes. Therefore, a comprehensive understanding of how roughness develops and evolves is fundamental for improving the fidelity of aerodynamic degradation predictions.

This study has two primary objectives. First, we extend the validation of the model presented by Zabaleta *et al.* (2024) by applying it to a more complex configuration: a swept tail. Second, we use the validated model to investigate collection efficiency on a laser-scanned geometry for which experimental impingement data are not available. The remainder of this brief is structured as follows: The numerical model is described in Section 2, followed by the swept tail validation in Section 3. The investigation of the laser-scanned rime ice geometry is presented in Section 4, and conclusions are drawn in Section 5.

2. Numerical model

The numerical simulations are conducted using the computational fluid dynamics code charLES, a low-dissipation, finite-volume solver (Brès *et al.* 2018). This work solves the low-pass filtered, compressible Navier–Stokes equations for mass, momentum, and total energy,

$$\frac{\partial \overline{\rho}}{\partial t} + \frac{\partial \overline{\rho}\tilde{u}_i}{\partial x_i} = 0, \tag{2.1}$$

$$\frac{\partial \overline{\rho}\tilde{u}_i}{\partial t} + \frac{\partial \overline{\rho}\tilde{u}_i\tilde{u}_i}{\partial x_i} = -\frac{\partial \overline{p}}{\partial x_i} + \frac{\partial \tilde{\tau}_{ij}}{\partial x_i} - \frac{\partial \tilde{\tau}_{ij}^{sgs}}{\partial x_i}, \tag{2.2}$$

$$\frac{\partial \overline{E}}{\partial t} + \frac{\partial \tilde{u}_i\overline{E}}{\partial x_i} + \frac{\partial \tilde{u}_i\overline{p}}{\partial x_i} = \frac{\partial \tilde{\tau}_{ij}\tilde{u}_i}{\partial x_i} - \frac{\partial \tilde{\tau}_{ij}^{sgs}\tilde{u}_i}{\partial x_i} + \frac{\partial}{\partial x_i}\left(\lambda\frac{\partial \overline{T}}{\partial x_i}\right) - \frac{\partial \tilde{Q}_i^{sgs}}{\partial x_i}, \tag{2.3}$$

where the operators $\overline{(\cdot)}$ and $\tilde{(\cdot)}$ represent filtered and Favre (density-weighted) filtered quantities, respectively. In these equations; u_i stands for the velocity vector; p represents the pressure; ρ is the density; τ_{ij} and τ_{ij}^{sgs} represent the viscous and subgrid stresses, respectively; E stands for the total energy; T is the temperature; λ is the thermal conductivity; and Q_i^{sgs} represents the subgrid heat flux. The subgrid terms are closed using the dynamic Smagorinsky model (Germano *et al.* 1991; Moin *et al.* 1991), and pressure, density, and temperature are related by the ideal gas law.

Time integration is achieved using a five-stage explicit Runge–Kutta scheme, while spatial discretization is performed with second-order accurate schemes using skew-symmetric operators that conserve kinetic energy in the inviscid, zero Mach number limit, and also approximately preserve entropy in the inviscid, adiabatic limit (Honein & Moin 2004; Chandrashekar 2013). Given the high Reynolds number, an algebraic wall model is employed to calculate wall shear stress, enabling accurate results while maintaining a reasonable computational cost (Lehmkuhl *et al.* 2018).

2.1. *Particle-tracking solver*

The dynamics of the dispersed phase (droplets) are described using a one-way coupled Lagrangian particle approach. This approach is suitable for aircraft icing simulations because of the low volumetric concentrations of droplets, allowing droplet effects on the airflow and droplet–droplet interactions to be neglected (Balachandar & Eaton 2010).

The trajectory of each individual particle is computed by integrating Newton's second law,

$$\frac{dx_{p,i}^k}{dt} = u_{p,i}^k, \tag{2.4}$$

$$m_p^k \frac{du_{p,i}^k}{dt} = -f_i^k, \tag{2.5}$$

where $x_{p,i}^k$ is the position vector of the kth particle, $u_{p,i}^k$ is the particle's velocity, m_p^k is the mass of the particle, and f_i^k represents the interaction forces between the particle and the fluid. Due to the high density ratio (ρ_p/ρ) and the high disparity between freestream velocity and settling velocity, the momentum transfer is dominated by the drag force (Guardone *et al.* 2025). The interaction force is modeled using the drag correlation presented by Schiller & Naumann (1935),

$$f_i^k = 3\pi\mu d_p^k \left(1 + 0.15 Re_p^{0.687}\right)\left(u_{p,i}^k - u_i\right), \tag{2.6}$$

where d_p^k is the particle diameter and $Re_p = \rho d_p (u_{p,i}^k - u_i)/\mu$ is the particle Reynolds number.

2.2. *Collection efficiency and splashing model*

The parameter that describes the impingement rate of particles over the geometry is the collection efficiency, β. It is defined as the ratio of droplet mass flux at the body surface ($\dot{m}_s$) to the freestream mass flux ($\dot{m}_\infty$). The collection efficiency, in a Lagrangian framework, is calculated as

$$\beta = \frac{\dot{m}_s}{\dot{m}_\infty}, \quad \dot{m}_s = \lim_{t\to\infty} \frac{1}{dA_s t} \sum_{k=1}^{N_s(t)} m_p^k, \quad \dot{m}_\infty = U_\infty \mathrm{LWC}, \tag{2.7}$$

where t is the simulation time, dA_s is an infinitesimal area on the impact surface, and $N_s(t)$ is the number of particles impacting dA_s at time t. In these simulations, dA_s represents the area of a boundary face. The triangle-trajectory intersection algorithm developed by Möller & Trumbore (2005) is employed to detect collisions between the particle and the surface mesh.

Droplet–wall interactions are critical in supercooled large-droplet (SLD) icing conditions. Following impact, droplets exhibit one of three behaviors: adhesion to the surface, rebounding, or splashing into multiple secondary droplets. When rebounding or splashing occurs, water mass is returned to the airflow, directly affecting the net collection rate. The likelihood and extent of splashing depend on droplet material properties (density, viscosity, surface tension), kinematic conditions (size, impact velocity), and geometric factors (impact angle). Generally, larger droplets impacting at higher velocities produce more intense splashing, while shallower impact angles and reduced impact frequencies enhance the tendency to splash.

The splashing model presented by Wright (2006), widely used in ice accretion prediction (Wright *et al.* 2008; Bellosta *et al.* 2023), is employed here. This framework treats rebounding as a limiting case of splashing where all impacting mass is ejected as a single secondary droplet with no surface adhesion. Splashing onset is governed by the dimensionless parameter K_L, defined as

$$K_L = \frac{0.859\sqrt{K}(\rho/\mathrm{LWC})^{0.125}}{\sin(\alpha)^{1.25}}, \tag{2.8}$$

where K is the Mundo parameter (Mundo *et al.* 1995), α is the impact angle, and K relates to the Ohnesorge number (Oh) and particle Reynolds number (Re_p) via

$$K = Oh Re_p^{1.25}. \tag{2.9}$$

For $K_L \leq 200$, complete adhesion occurs with no splashing. When $K_L > 200$, the splashed

mass fraction (Φ) is

$$\Phi = \frac{m_{\text{splash}}}{m_{\text{imp}}} = \begin{cases} 0 & K_L \leq 200 \\ 0.7(1-\sin\alpha)\left(1 - e^{-0.0092026(K_L - 200)}\right) & K_L > 200. \end{cases} \tag{2.10}$$

Secondary droplet properties (diameter and velocity components) follow from

$$\frac{d_{\text{splash}}}{d_{\text{imp}}} = 8.72e^{-0.0281K}, \tag{2.11}$$

$$u_{n,\text{splash}} = u_{n,\text{imp}}(0.3 - 0.002\alpha), \tag{2.12}$$

$$u_{t,\text{splash}} = u_{t,\text{imp}}(1.075 - 0.0025\alpha). \tag{2.13}$$

At each droplet–surface collision, K_L and Φ are computed to determine the outcome. The adhering mass fraction is accumulated on the impacted computational face, while the splashed fraction generates secondary droplets with properties given by Eq. (2.11). When splashing produces multiple secondary droplets, a parcel representation (Drew & Passman 1998) is used to maintain computational efficiency.

3. NACA 64A008 swept tail

While Zabaleta *et al.* (2024) demonstrated the model's accuracy in predicting collection efficiency for a two-dimensional airfoil, here we evaluate its performance on a three-dimensional geometry. The model is therefore validated against experiments on a NACA 64A008 swept tail, a three-dimensional case that was also part of the IPW 1.

3.1. *Computational setup*

The computational setup corresponds to experiments by Papadakis *et al.* (2002) for a clean NACA 64A008 swept tail at a 6° angle of attack in droplet clouds with median volume diameters (MVDs) of 21 and 92 μm. With a mean aerodynamic chord (MAC) of 36 inches and a freestream velocity of 78.68 m/s, the flow conditions yield a Reynolds number of 5 million and a Mach number of 0.23. The droplet distributions follow a 27-bin characterization, detailed in Table 1. Experimental data from NASA's Glenn Research Center include C_p distributions at midboard and outboard sections and collection efficiency measurements from blotter strips positioned 36 inches from the tunnel floor. The test section dimensions are 9 feet wide by 6 feet tall.

The mesh resolution is 1250 cells per MAC, resulting in a total cell count of 20 million control volumes. The computational domain extends 9 MAC streamwise, with cross-sectional dimensions matching the wind tunnel. Slip boundary conditions are applied to the lateral walls, freestream velocity is specified at the inlet, and a nonreflective condition is used at the outlet. Particles are introduced at a rectangular plane 0.5 MAC upstream of the airfoil base with freestream velocity and are removed upon passing the airfoil. Following Zabaleta *et al.* (2024), the 27-bin distribution is subsampled to seven representative bins, each simulated separately and then combined on their percentage of LWC. Approximately 60 million particles are injected per convective timescale (MAC/U_∞) to accelerate the convergence rate.

3.2. *Results*

The simulation was run to a statistically stationary state before introducing droplets into the domain. Statistical stationarity was achieved after 20 convective time units. Figure

		Droplet diameter (μm)				Droplet diameter (μm)	
Bin	LWC (%)	MVD = 21	MVD = 92	Bin	LWC (%)	MVD = 21	MVD = 92
1	4.75	4.0	10.8	15	4.75	25.7	121.8
2	4.75	8.8	24.4	16	4.75	27.1	130.6
3	4.75	10.3	29.8	17	4.75	28.8	140.6
4	4.75	11.8	35.2	18	4.75	30.8	152.3
5	4.75	13.2	42.0	19	4.75	34.4	165.6
6	4.75	14.7	51.4	20	4.75	47.9	187.6
7	4.75	16.1	61.5	21	1.00	61.9	209.6
8	4.75	17.4	69.9	22	1.00	68.7	226.1
9	4.75	18.5	77.5	23	1.00	76.9	247.1
10	4.75	19.7	84.7	24	0.50	84.8	265.7
11	4.75	20.8	91.7	25	0.50	92.4	290.3
12	4.75	22.0	98.8	26	0.50	103.4	339.5
13	4.75	23.2	106.2	27	0.50	164.0	391.8
14	4.75	24.4	113.9				

TABLE 1. Discretized droplet size distribution for clouds with median volume diameters (MVDs) of 21 μm and 92 μm. The table shows the liquid water content (LWC) in percent along with the representative droplet diameter for each bin.

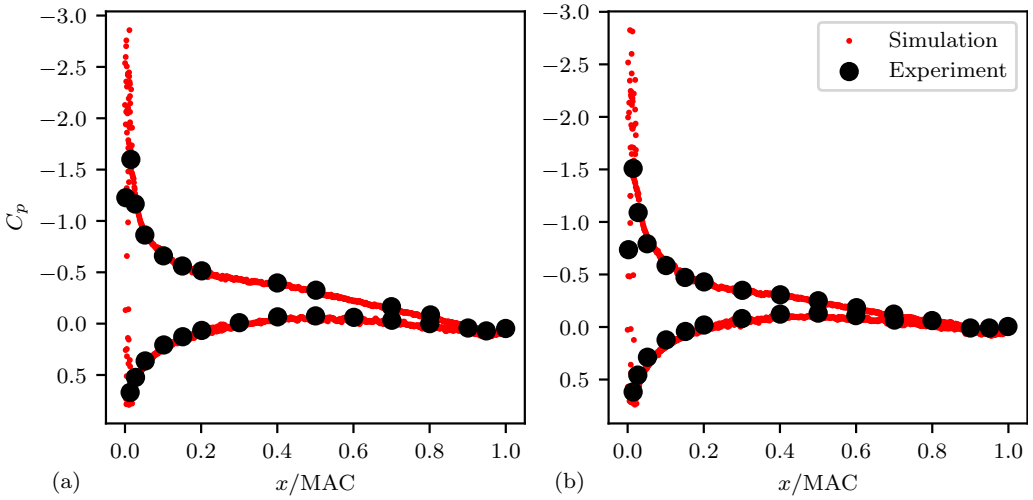

FIGURE 1. Pressure coefficient (C_p) obtained with the numerical model superimposed with the experimental values for the midboard (a) and the outboard (b) sections.

1 presents the C_p distributions for the midboard and outboard sections, demonstrating good agreement between the numerical model and experimental data and validating the aerodynamic part of the calculations.

Once the aerodynamic simulation reaches a statistically stationary state, particles are injected into the flow and the simulation is run for another 30 convective time units. Figure 2 compares the numerically predicted collection efficiency distributions with the experimental measurements by Papadakis *et al.* (2002) for the two cloud diameters. For the MVD 21 μm case, the numerical model demonstrates good overall agreement with the experimental data, correctly capturing the shape, peak, and impingement limits.

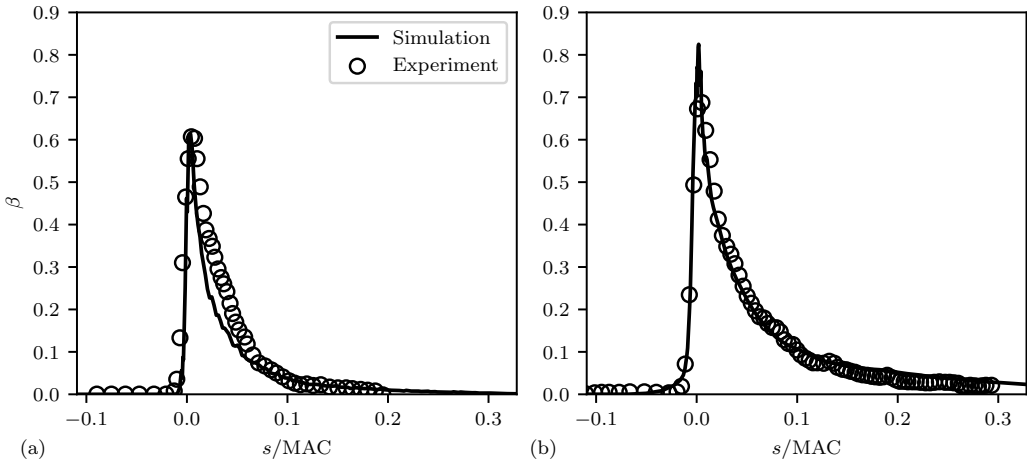

FIGURE 2. Collection efficiency distribution (β) as a function of the nondimensional streamwise coordinate s/MAC obtained with the numerical model superimposed with the experimental data from Papadakis *et al.* (2002) for the MVD = 21 μm cloud (a) and the MVD = 92 μm cloud (b).

A slight underprediction of the collection efficiency is observed near $s/\mathrm{MAC} = 0.03$. This discrepancy is consistent with similar findings from participants of the IPW 1. For the MVD = 92 μm case, the model's performance is excellent. The simulation results match the experimental data across the entire impingement region, accurately capturing the peak value of β and the subsequent distribution. This agreement is notably better than the results presented by most participants from the IPW 1 for this large-droplet condition. While the localized discrepancy near s/MAC=0.03 appears to fall outside the 12% experimental uncertainty band reported by Papadakis *et al.* (2002), the excellent agreement elsewhere, particularly for the SLD case of MVD = 92 μm, demonstrates the overall high accuracy of the model.

The predictive accuracy demonstrated here, in conjunction with the model's prior validation for the NACA 23012 airfoil by Zabaleta *et al.* (2024), provides a strong foundation and high confidence in the model's capability to predict droplet impingement. This validation allows us to explore droplet impingement in more complex scenarios for which validation data are not available.

4. Laser-scanned rime ice

Following successful validation on clean geometries, the model is now applied to predict droplet impingement on a realistic, laser-scanned ice shape. This section aims to investigate how complex three-dimensional surface features, such as roughness, influence the collection efficiency distribution, particularly for cases where such experimental data are unavailable.

4.1. *Computational setup*

The geometry for this analysis is the laser-scanned rime ice on a NACA 23012 airfoil from the experiments performed by Broeren *et al.* (2018), specifically Case ED1977. While previous work successfully predicted the aerodynamic degradation for this case (Bornhoft *et al.* 2024), the current investigation focuses on the droplet impingement characteristics—a type of data not measured in the original experiment. To isolate the

influence of the measured three-dimensional roughness, simulations are performed on both the authentic laser-scanned geometry and an equivalent smooth body, which was generated by extruding the mean cross section of the ice shape. The airfoil has an 18-inch chord (c) and is at a 2° angle of attack.

The computational domain extends seven chord lengths in the streamwise direction and has a spanwise width of $1c$. A mean freestream velocity of $U_\infty = 102.8\,\mathrm{m/s}$ is specified at the inlet, while a nonreflective condition is applied at the outlet. The top and bottom boundaries are treated as slip walls, and periodic boundary conditions are used in the spanwise direction. The mesh resolution was set to approximately 5010 cells per chord length, with a finer resolution in the leading edge. This grid density is considerably finer than that required to achieve accurate aerodynamic load predictions (Bornhoft *et al.* 2024); however, this high resolution was deliberately chosen to ensure that the small-scale roughness features were adequately resolved, which is critical for capturing their effect on the local collection efficiency, β.

To investigate the influence of droplet size on impingement characteristics over the rough surface, simulations were performed for six different monodisperse droplet diameters: 5, 10, 20, 40, 80, and 120 μm.

For the particle-tracking phase, droplets are introduced at an injection plane located $0.5c$ upstream of the airfoil's leading edge. This rectangular injection area covers the full span of the domain and has a height of $0.22c$. Individual particles are seeded at random locations within this plane. The trajectory of each particle is tracked until it either intersects the airfoil surface or passes the airfoil trailing edge.

4.2. *Results*

The initial step in the analysis is to quantify the effect of the three-dimensional surface roughness on the spanwise-averaged collection efficiency. Figure 3 presents the spanwise-averaged collection efficiency, β, for both the laser-scanned rough geometry and its smooth, extruded counterpart across all six simulated droplet diameters. The results show that, for nearly all conditions, the collection efficiency distributions are virtually identical, indicating that the surface roughness has a negligible effect on the spanwise-averaged impingement. The only minor deviation occurs for the largest droplet diameters near $s/c = -0.2$, which coincides with the end of the roughness. This finding explains the success of many ice accretion models predicting mean rime ice shapes while neglecting surface roughness. The accuracy of these models depends on capturing the correct total impinging water mass; our finding confirms that this prerequisite is met, as the spanwise-averaged collection efficiency is found to be independent of roughness.

Although the mean collection efficiencies are unaltered by the presence of roughness, the local distribution of impinging droplets varies significantly, as shown in the collection efficiency maps in Figure 4. For the smooth profile, the collection efficiency is almost entirely uniform in the spanwise direction. In contrast, the laser-scanned geometry exhibits a highly nonuniform impingement pattern that clearly correlates with the underlying surface roughness. This effect is strongly dependent on droplet diameter. For small droplets (<10 μm), which impinge primarily near the leading edge, the influence of the downstream roughness is limited. As the droplet diameter increases, however, the impingement region widens, and the effect of the surface roughness becomes much more pronounced, with the collection efficiency distribution mirroring the texture of the rough ice.

A closer analysis of the local impingement on the rough geometry reveals that droplet collection is concentrated on the upstream-facing faces of the individual roughness ele-

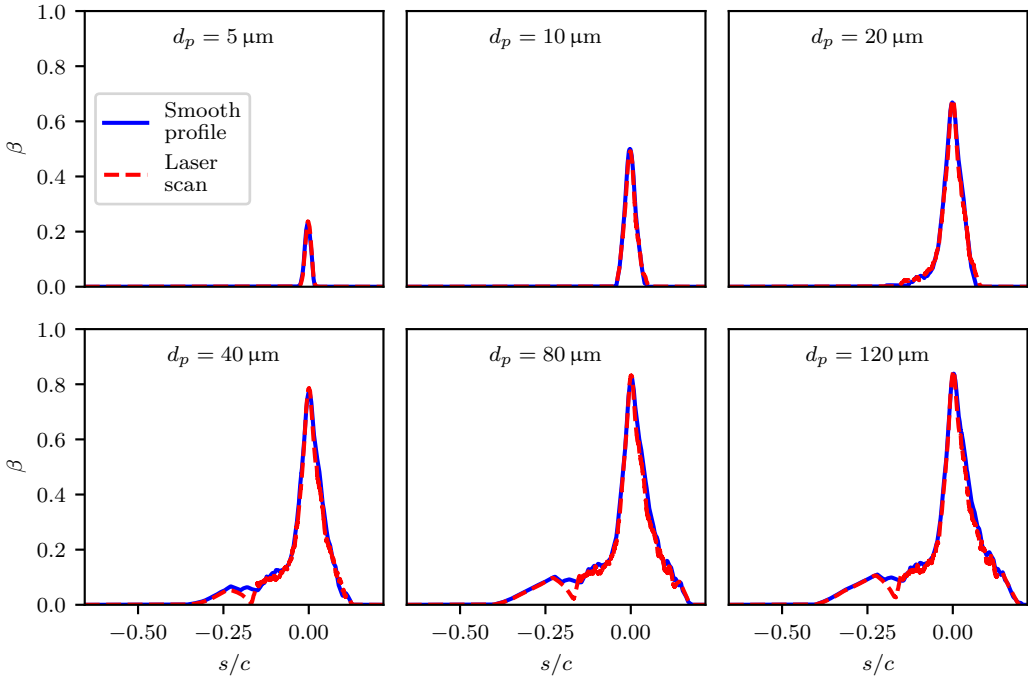

FIGURE 3. Comparison of the spanwise-averaged collection efficiency (β) between the laser-scanned rough geometry and the smooth mean section for six different droplet diameters.

ments. These elements effectively intersect the incoming droplets, creating a sheltered zone immediately behind them, where the local collection efficiency approaches zero. This phenomenon is critical for the subsequent ice accretion process. The preferential deposition of mass on the frontal area of the existing roughness elements promotes their continued growth in the upstream direction.

The impact of surface roughness on ice accretion dynamics is illustrated in Figure 5, which compares the predicted ice growth after 1 min for both the smooth and laser-scanned geometries using the methodology from Zabaleta *et al.* (2025b). These results provide compelling evidence for the self-reinforcing nature of surface roughness in ice accretion processes. For the initially smooth surface, the simulated ice growth maintains a relatively uniform profile. While there is a slight thickening of the ice layer, the overall shape closely follows the contours of the original geometry, with minimal development of new surface features. In contrast, the laser-scanned rough surface exhibits a remarkably different growth pattern. The simulation predicts that existing roughness features not only persist but are actually amplified during the accretion process. The initially rough profile becomes even more irregular, with pronounced protrusions and indentations developing along the surface.

This divergence in growth patterns can be attributed to the localized variations in collection efficiency observed earlier. On the rough surface, the preferential deposition of droplets on upstream-facing features leads to accelerated growth in these areas, while the sheltered regions experience reduced accretion. As a result, the roughness elements grow preferentially in the upstream direction, exaggerating the existing surface irregularities. This mechanism provides a physical explanation for the formation and growth of characteristic rime ice structures, such as feathers, and underscores the importance of ac-

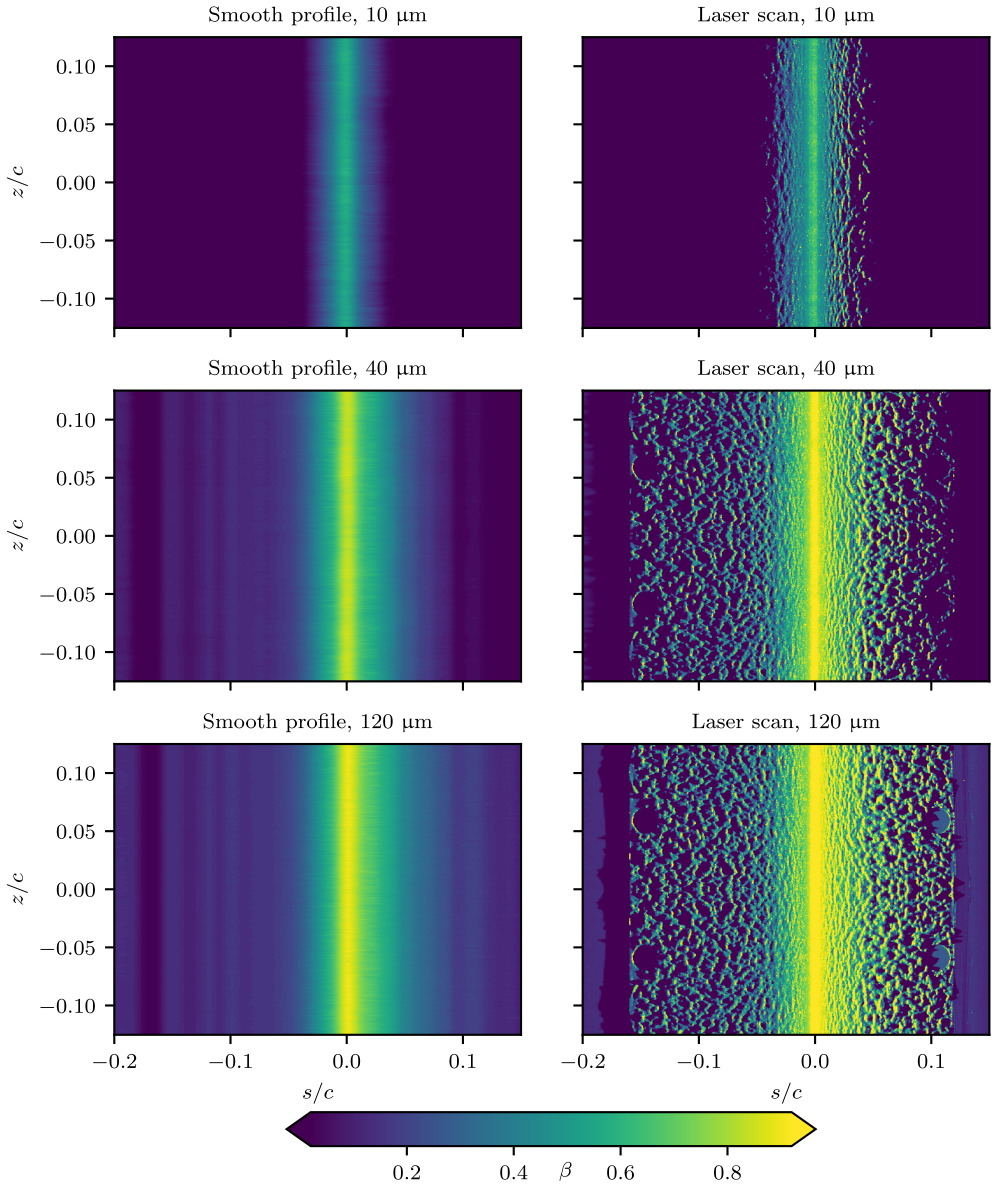

FIGURE 4. Collection efficiency (β) maps for the laser-scanned rough geometry (right) and the smooth mean section (left) for three different droplet diameters (10 µm, 40 µm, and 120 µm).

curately modeling local surface geometry in ice accretion simulations. Furthermore, these findings suggest that even small initial perturbations in surface smoothness could lead to significant roughness development over time, highlighting the potential limitations of models that rely on idealized, smooth geometries for long-term ice growth predictions.

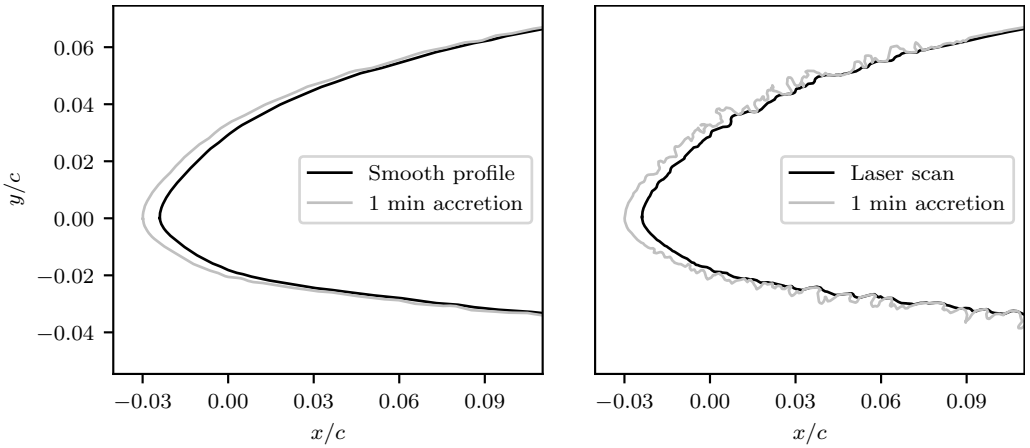

FIGURE 5. Comparison of predicted ice accretion after 1 min on smooth and laser-scanned rough surfaces.

5. Conclusions

This study presents calculations of droplet impingement using high-fidelity numerical simulations. Our approach, which combines wall-modeled large-eddy simulations with a Lagrangian particle model, has been successfully validated against experimental data for a NACA 64A008 swept tail, extending its applicability to complex three-dimensional geometries. The model demonstrates excellent agreement with experimental collection efficiency distributions, particularly for large-droplet conditions.

By performing numerical simulations on laser-scanned geometries, we showed that surface roughness significantly impacts local droplet impingement distributions. While spanwise-averaged collection efficiency remains largely unaffected by surface roughness, substantial local variations are observed, particularly in rough regions and for larger droplets. Droplet collection efficiency is concentrated on the upstream-facing surfaces of roughness elements, creating sheltered zones with near-zero collection efficiency immediately behind these features.

Our simulations reveal a self-reinforcing mechanism of roughness growth that is driven by the local surface geometry. Droplets preferentially deposit on the upstream-facing faces of existing roughness elements, which in turn create sheltered zones immediately downstream, where impingement approaches zero. This preferential deposition promotes the continued growth of the roughness elements themselves, providing a physical explanation for the formation of characteristic rime ice feathers. These findings have significant implications for ice accretion modeling. They suggest that, in order to accurately predict the development and evolution of these features, models must account for small-scale surface perturbations, as even minor initial irregularities can be amplified by this self-reinforcing process.

Acknowledgments

This investigation was funded by Boeing and NASA's Transformational Tools and Technologies Project. This research used resources of the Oak Ridge Leadership Computing Facility, which is a US Department of Energy, Office of Science, User Facility supported under contract DE-AC0500OR22725. The authors thank Ahmed Elnahhas for his insightful comments on this report.

REFERENCES

Balachandar, S. & Eaton, J. K. 2010 Turbulent dispersed multiphase flow. *Annu. Rev. Fluid Mech.* **42**, 111–133.

Bellosta, T., Baldan, G., Sirianni, G. & Guardone, A. 2023 Lagrangian and Eulerian algorithms for water droplets in in-flight ice accretion. *J. Comput. Appl. Math.* **429**, 115230.

Bellosta, T., Donizetti, A., Zabaleta, F., Bornhoft, B., Jain, S. S., Bose, S. T. & Guardone, A. 2024 Assessing relevant roughness scales for accurate prediction of iced airfoil aerodynamics. *Proceedings of the 2024 Summer Program*, Center for Turbulence Research, Stanford University, pp. 427–437.

Bornhoft, B., Jain, S. S., Goc, K., Bose, S. T. & Moin, P. 2024 Large-eddy simulations of the NACA23012 airfoil with laser-scanned ice shapes. *Aerosp. Sci. Technol.* **146**, 108957.

Bornhoft, B., Moin, P., Jain, S. S. & Bose, S. T. 2025 On the use of artificial ice shapes for large-eddy simulations in aircraft icing. *J. Aircr.* `https://doi.org/10.2514/1.C038146`.

Brès, G. A., Bose, S. T., Emory, M., Ham, F. E., Schmidt, O. T., Rigas, G. & Colonius, T. 2018 Large-eddy simulations of co-annular turbulent jet using a Voronoi-based mesh generation framework. *AIAA Paper 2018-3302*.

Broeren, A. P., Addy, H. E., Lee, S., Monastero, M. C. & McClain, S. T. 2018 Three-dimensional ice-accretion measurement methodology for experimental aerodynamic simulation. *J. Aircr.* **55**, 817–828.

Chandrashekar, P. 2013 Kinetic Energy preserving and entropy stable finite volume schemes for compressible Euler and Navier-Stokes equations. *Commun. Comput. Phys.* **14**, 1252–1286.

Drew, D. A. & Passman, S. L. 1998 *Theory of Multicomponent Fluids*. Springer.

Gent, R. W., Dart, N. P. & Cansdale, J. T. 2000 Aircraft icing. *Philos. Trans. R. Soc. Lond. A* **358**, 2873–2911.

Germano, M., Piomelli, U., Moin, P. & Cabot, W. H. 1991 A dynamic subgrid-scale eddy viscosity model. *Phys. Fluids A* **3**, 1760–1765.

Guardone, A., Bellosta, T., Donizetti, A. & Gallia, M. 2025 Aircraft icing: modeling and simulation. *Annu. Rev. Fluid Mech.* **58**. In press.

Honein, A. E. & Moin, P. 2004 Higher entropy conservation and numerical stability of compressible turbulence simulations. *J. Comput. Phys.* **201**, 531–545.

Ignatowicz, K., Morency, F. & Beaugendre, H. 2023 Surface roughness in RANS applied to aircraft ice accretion simulation: a review. *Fluids* **8**, 278.

Laurendeau, E., Bourgault-Cote, S., Ozcer, I. A., Hann, R., Radenac, E. & Pueyo, A. 2022 Summary from the 1st AIAA Ice Prediction Workshop. *AIAA Paper 2022-3398*.

Lehmkuhl, O., Park, G. I., Bose, S. T. & Moin, P. 2018 Large-eddy simulation of practical aeronautical flows at stall conditions. *Proceedings of the Summer Program*, Center for Turbulence Research, Stanford University, pp. 87-96.

Messinger, B. L. 1953 Equilibrium temperature of an unheated icing surface as a function of air speed. *J. Aeronaut. Sci.* **20**, 29–42.

Moin, P., Squires, K., Cabot, W. & Lee, S. 1991 A dynamic subgrid-scale model for compressible turbulence and scalar transport. *Phys. Fluids A* **3**, 2746–2757.

Möller, T. & Trumbore, B. 2005 Fast, minimum storage ray/triangle intersection. In *SIGGRAPH '05: ACM SIGGRAPH 2005 Courses*, pp. 1–7. ACM.

Mundo, C., Sommerfeld, M. & Tropea, C. 1995 Droplet-wall collisions: experimental studies of the deformation and breakup process. *Int. J. Multiph. Flow* **21**, 151–173.

Myers, T. G. 2001 Extension to the Messinger model for aircraft icing. *AIAA J.* **39**, 211–218.

National Transportation Safety Board 2023 Aviation accidents: index of months. `https://www.ntsb.gov/safety/Pages/research.aspx`.

Ozcer, I. A., Baruzzi, G. S., Reid, T., Habashi, W. G., Fossati, M. & Croce, G. 2011 FENSAP-ICE: numerical prediction of ice roughness evolution, and its effects on ice shapes. In *SAE 2011 International Conference on Aircraft and Engine Icing and Ground Deicing*. SAE.

Papadakis, M., Hung, K. E., Vu, G. T., Yeong, H. W., Bidwell, C. S., Breer, M. D. & Bencic, T. J. 2002 Experimental investigation of water droplet impingement on airfoils, finite wings, and an S-duct engine inlet. Tech. Rep. 20020090796, NASA.

Petty, K. & Floyd, C. D. J. 2004 Statistical review of aviation airframe icing accidents in the U.S. In *Proceedings of the 11th Conference on Aviation, Range, and Aerospace Meteorology*. American Meteorology Society.

Schiller, L. & Naumann, A. 1935 A drag coefficient correlation. *Z. Ver. Dtsch. Ing.* **77**, 318–320.

Shad, A., Ahmed, H., Zgheib, N., Balachandar, S. & Sherif, S. A. 2025 Stokes-dependent droplet collection efficiency on a NACA 0012 airfoil from droplet-informed simulations with statistical overloading. *Philos. Trans. R. Soc. Lond. A* **383**, 20240368.

Wright, W. 2006 Further refinement of the LEWICE SLD model. *AIAA Paper 2006-0464*.

Wright, W., Potapczuk, M. & Levinson, L. 2008 Comparison of LEWICE and GlennICE in the SLD regime. *AIAA Paper 2008-0439*.

Zabaleta, F., Bornhoft, B., Jain, S. S., Bose, S. T. & Moin, P. 2025a Large-eddy simulations of conjugate heat transfer in boundary layers over laser-scanned ice roughness. *Phys. Rev. Fluids* **10**, 104603.

Zabaleta, F., Jain, S. S., Bornhoft, B. J., Bose, S. & Moin, P. 2024 Large-eddy simulation of supercooled large droplets impingement using a Lagrangian particle approach. *AIAA Paper 2024-4162*.

Zabaleta, F., Yu, H. & Moin, P. 2025b Multishot simulations of rime ice accretion. *Annual Research Briefs*, Center for Turbulence Research, Stanford University, pp.143-155.